Rheol Acta (2007) 46:1171–1186
DOI 10.1007/s00397-007-0199-2

ORIGINAL CONTRIBUTION

A molecular dynamics study of the stress–optical behavior of a linear short-chain polyethylene melt under shear

Chunggi Baig · Brian J. Edwards · David J. Keffer

Received: 26 March 2006 / Accepted: 26 April 2007 / Published online: 22 May 2007

Abstract In this study, we present details of the stress–optical behavior of a linear polyethylene melt under shear using a realistic potential model. We demonstrate the existence of the critical shear stress, above which the stress–optical rule (SOR) begins to be invalid. The critical shear stress of the SOR of this melt turns out to be 5.5 MPa, which is fairly higher than 3.2 MPa at which shear thinning starts, indicating that the SOR is valid up to a point well beyond the incipient point of shear thinning. Furthermore, contrary to conventional wisdom, the breakdown of the SOR turns out not to be correlated with the saturation of chain extension and orientation: It occurs at shear rates well before maximum chain extension is obtained. In addition to the stress and birefringence tensors, we also compare two important coarse-grained second-rank tensors, the conformation and orientation tensors. The birefringence, conformation, and orientation tensors display nonlinear relationships to each other at high values of the shear stress, and the deviation from linearity begins at approximately the critical shear stress for breakdown of the SOR.

Keywords Birefringence · Stress–optical rule · Shear · Nonequilibrium molecular dynamics · Linear polyethylene melt

Introduction

Optical measurement of the anisotropy of materials has proven to be very informative and useful in characterizing the structure and stress of molecular crystals (Vuks 1966; de Jong et al. 1991) and as a noninvasive tool in the study of rheology of polymeric fluids (Morrison 2001; Janeschitz-Kriegl 1983). There are generally two types of birefringence, form birefringence and flow birefringence. The former originates from the difference in the intrinsic (average) polarizability between the solvent and polymer, and the latter from anisotropic orientation of polymer chain bonds induced by the flow (Doi and Edwards 1986). Accordingly, form birefringence is expected to make a significant contribution to the total birefringence in dilute polymer solutions, providing us with information about the nonspherical shape of polymer aggregates in solutions. However, it can be ignored in concentrated polymer solutions or melts, for which flow birefringence is the dominant effect. Because flow birefringence is directly determined by a preferred orientation of molecules (bonds) in space under an externally imposed flow field, it would, in general, depend on specific polymers (and possibly their molecular weights), the detailed kinematics of the flow (type and strength), and system conditions (such as temperature and density).

An important application of birefringence to the rheology of polymer melts under flow comes from the supposition that there exists a certain relationship between the anisotropy of birefringence and that of stress, that is, the stress–optical behavior. A well-known fact is that there exists, under a wide variety of conditions, a linear relationship between the stress tensor σ and the real part of the refractive index tensor, or "birefringence tensor," n, which is the so-called stress–optical rule (SOR), $\Delta n = C\Delta\sigma$. Here, C is called the "stress–optical coefficient" and the birefringence Δn is the difference between the principal components of the real part of the refractive index tensor.

To date, there are numerous experimental works examining the SOR. One of the first detailed experimental

C. Baig · B. J. Edwards (✉) · D. J. Keffer
Department of Chemical Engineering, University of Tennessee, Knoxville, TN 37996-2200, USA
e-mail: bje@utk.edu

studies of the stress–optical behavior of amorphous polymers was carried out by Matsumoto and Bogue (1977) using polystyrene melts at temperatures above the glass transition temperature T_g. These experiments were conducted under both isothermal and nonisothermal conditions. The polymer samples were uniaxially elongated using a mechanical–optical apparatus. They obtained a master stress–birefringence curve on which all the data from both isothermal and nonisothermal conditions were superimposed. They reported that the SOR began to fail at stress values larger than about 1 MPa.

Since then, more extensive experimental studies of the SOR have been performed using more elaborate elongational stress–optical apparati (Muller and Froelich 1985; Inoue et al. 1991; Kotaka et al. 1997; Okamoto et al. 1998; Venerus et al. 1999). Muller and Pesce (1994) observed significant deviations from the SOR at temperatures near T_g in both polystyrene and polycarbonate melts undergoing uniaxial elongation. They reported that at high temperatures (i.e., above T_g+20 K), the stress–optical behavior of the polymer melts was independent of temperature and strain rate in the nonlinear regime as well as the linear regime where the SOR is valid. Inoue et al. (1996) investigated the stress–optical behavior of several vinyl polymers from the glassy to the rubbery regions through dynamic birefringence measurements.

Recently, incorporating an optical measurement device into an advanced elongational rheometer developed by Meissner and Hostettler (1994), Venerus et al. (1999) carried out a very careful stress–optical study and re-examined the stress–optical behavior of polystyrene melts under uniaxial elongational flow at sufficiently high temperatures, above T_g+60 K. They reported that C of the polystyrene melt was 4.8×10^{-9} Pa^{-1} and that the critical stress for the breakdown of the SOR was roughly 1 MPa. These results are in good agreement with other previously reported values (Muller and Froelich 1985; Janeschitz-Kriegl 1983). They also observed that C decreases with increasing extensional stress, consistent with many existing results. Some time ago, Kotaka et al. (1997), however, reported the opposite behavior of polystyrene melts (but not polyethylene melts) that C increases with increasing extensional stress. In this regard, Venerus et al. (1999) speculated that in the experiments of Kotaka et al. (1997) with polystyrene melts, a necking process might have developed, causing the measured stress to decrease while the birefringence was not sufficiently relaxed.

More recently, also using polystyrene melts under elongation but with narrow molecular weight distributions, Luap et al. (2005) reported that the critical stress of the SOR was about 2.7 MPa, independent of temperature and strain rate, and it corresponded to a Weissenberg number $\left(We = \lambda\dot{\gamma}\right)$ approximately equal to 3. (The temperatures employed in their study were above T_g+40 K.) They also showed that the SOR was valid well into the strain-thinning region of nonlinear flow behavior. By comparing theoretical predictions with existing experimental findings, Van Meerveld (2004) analyzed the effect of the molecular weight distribution on the critical stress value for breakdown of the SOR, based on the idea that deviations to the SOR were effectively determined by the number of stretched chains in the melt. In the meantime, Cormier and Callaghan (2002) applied another new experimental technique, which combines rheometry with magnetic resonance imaging spectroscopy, to measure segmental alignment in polymer melts under shear flow. Because it is expected to become more and more advanced in the future, this technique seems to be very promising in the rheo-optical study of polymer melts under various flows. On the theoretical side, Palierne (2004) demonstrated that the full Doi–Edwards reptation model predicts the failure of the SOR at large shear strains, although a restricted version using the so-called independent alignment approximation still guarantees that the SOR is valid.

There have also been a few computer simulation studies of the stress–optical behavior of polymer melts. Kröger et al. (1993, 1997) investigated the stress–optical behavior of polymer melts under shear (Kröger et al. 1993) and uniaxial elongation flow (Kröger et al. 1997) using a multi-bead anharmonic-spring model. They reported the breakdown of the SOR at high strain rates for both types of flows. More realistic potential models have been employed in simulation studies of polyethylene melts under uniaxial elongation by Gao and Weiner (1994) using molecular dynamics simulations, and later by Mavrantzas and Theodorou (2000a, b) using their advanced Monte Carlo technique (the so-called end-bridging Monte Carlo simulation). Mavrantzas and Theodorou (2000b) observed the change of C with chain length, with a plateau value obtained for chain lengths greater than $C_{400}H_{802}$.

Much of the previous work (both experiments and simulations) on the stress–optical behavior has been performed with uniaxial elongational flow rather than shear flow. It seems to be mainly due to an experimental difficulty in achieving sufficiently high shear stress values to observe the failure of the SOR because of undesirable side effects such as melt fracture, nonuniform birefringence distribution because of frictional heat production, and parasitic birefringence near the optical windows (Janeschitz-Kriegl 1983). This might have led people to think that the SOR would be valid for shear flow, although Kröger et al. (1993) reported the failure of the SOR in the case of the multibead spring melts under shear. Therefore, a definitive statement concerning the breakdown of the SOR of polymer melts under shear flow seems to be necessary at this point, which has motivated the current work. To this end, computer

simulations are thought to be the most appropriate tool at present because the shear stress (or equivalently shear rate) employed in simulations can be much higher than that in practical experiments.

Another point worthy of investigation is the customary view that the SOR is likely to break down at very high stresses because of the saturation of chain extension and orientation (Treloar 1975; Morrison 2001; Janeschitz-Kriegl 1983). In fact, owing to its intrinsic kinematics, elongational flow makes chains become much more extended and oriented than shear flow. That is, in shear flow, chains are not likely to be stretched to such a high degree as in elongational flow, partly because of the rotational nature of shear. Therefore, the breakdown of the SOR under shear would not necessarily imply that the customary view is correct. This aspect is also considered in this study.

Herein, we further investigate the relationship between the birefringence and two structural properties that have been regarded as very important in a coarse-grained level of description (Beris and Edwards 1994): One is the conformation tensor $\tilde{c}$ and the other the orientation tensor u. It is easily seen from their definitions that the two are closely related to each other:

$$\tilde{c} = \frac{3\langle RR\rangle}{\langle R^2\rangle_{\mathrm{eq}}}, \tag{1}$$

$$u = 3\langle \hat{r}\hat{r}\rangle, \tag{2}$$

where $\boldsymbol{R}$ and $\hat{r}$ represent the chain end-to-end vector and unit vector along the chain end-to-end direction, respectively. Notice that the two tensors become the unit second-rank tensor at equilibrium. It might be thought that the birefringence tensor would be proportional to the conformation and orientational tensors at all strain rates. However, as we will see later in this article, this is not necessarily true.

Theoretical background for birefringence studies

To calculate the birefringence tensor of anisotropic materials, we first need to calculate the polarizability tensor of the system directly from the simulation and then the birefringence tensor from the calculated polarizability tensor using an appropriate theoretical formula. For isotropic materials, an exact formula exists, which is called the Clausius–Mossotti equation (see Eq. 9 below). Under quiescent conditions, this equation is adequate; however, under flow, the system of chain molecules will become anisotropic. For anisotropic materials, to the authors' knowledge, there does not seem to have appeared in the literature (before 2000) an exact generalized tensorial formula, although there have appeared several derivations of certain approximate formula applied in the study of molecular crystals (Vuks 1966; Urano and Inoue 1976; de Jong et al. 1991). Moreover, Mavrantzas and Theodorou (2000a) presented an anisotropic version of the exact formula, but no derivation of it was given in their article. In this study, we offer a derivation of this expression for anisotropic media, for completeness. The generalized Clausius–Mossotti tensorial formula for anisotropic materials reduces to the conventional Clausius–Mossotti equation for isotropic systems. We will also present in detail a procedure to calculate the polarizability tensor of molecules making use of their bond polarizability through a local coordinate transformation.

A derivation of the Clausius–Mossotti equation for anisotropic media

For easier comprehension of the anisotropic derivation below, we first derive the Clausius–Mossotti equation for isotropic materials. Consider a linear dielectric medium consisting of spherically symmetric nonpolar atoms (such as argon), or molecules (like methane). The polarization vector (dipole moment per unit volume) $\boldsymbol{P}$ of a linear dielectric material is proportional to the local electric field, denoted by E:

$$P = \varepsilon_0 \chi_{\mathrm{e}} E. \tag{3}$$

In this expression, ε_0 is the permittivity of a vacuum with the value of $8.854 \times 10^{-12}\ \mathrm{C}^2(\mathrm{N\ m}^2)^{-1}$ and χ_{e} is the electric susceptibility. In linear dielectric materials, χ_{e} is equal to $\varepsilon_{\mathrm{r}} - 1 = \varepsilon/\varepsilon_0 - 1$, where $\boldsymbol{\varepsilon}$ is the permittivity of the material and $\boldsymbol{\varepsilon}_{\mathrm{r}}$ is called the relative permittivity or the dielectric constant of the material (Griffiths 1999). The induced dipole moment of molecule i, denoted by p_i, is written as

$$p_i = \alpha_i E_{\mathrm{a}}, \tag{4}$$

where α_i is the polarizability of molecule i and E_{a} represents the applied electric field. Because we are currently dealing with identical and spherically symmetric molecules, we can simply designate $p_i{=}p$ and $\alpha_i{=}\alpha$ (it should be noted that the polarizability α should be, in general, regarded as a second-rank tensor for nonsymmetric molecules, as shown for anisotropic materials below). Note that for these spherical molecules, p and E_{a} lie in the same direction.

E will be, in general, different from E_{a} because at any point in space, there would be not only E_{a} but also an induced electric field, denoted by $\boldsymbol{E}_{\mathrm{d}}$. This field results from the induced dipoles inside an infinitesimally small (but still macroscopic in the sense that it contains many molecules) volume of interest. Consequently, $E{=}E_{\mathrm{a}}{+}E_{\mathrm{d}}$. It should be

also noted that in this material, E_d would lie in the opposite direction to E_a.

Suppose that there are N molecules in a small volume V of interest. If we take V as the local volume of the material, E_a in this volume will be the electric field including both the externally applied field and the field induced by only the dipoles outside the volume. In other words, E_a is the electric field due to everything except the dipoles inside the volume. (It might also be possible to take E_a as a field due to everything except the molecule under consideration.) For the number density of molecules $\tilde{N} = N/V$ in the volume under consideration, the polarization can be written as

$$P = \frac{1}{V}\sum_{i=1}^{N} p_i = \frac{Np}{V} = \tilde{N}p = \tilde{N}\alpha E_a. \tag{5}$$

In this equation, the second equality comes from the assumption that every molecule is identical and spherically symmetric and therefore has the same dipole moment. To derive the relationship between α and χ_e or ε_r, we need to know the induced electric field E_d because of the molecules inside the volume under consideration. It is well known that the field created by the dipoles is (Griffiths 1999)

$$E_d = -\frac{P}{3\varepsilon_0} = -\frac{\tilde{N}\alpha}{3\varepsilon_0}E_a, \tag{6}$$

where Eq. 5 was used for the second equality. Therefore, the local electric field E is then

$$E = E_a + E_d = \left(1 - \frac{\tilde{N}\alpha}{3\varepsilon_0}\right)E_a. \tag{7}$$

If we substitute Eq. 7 into Eq. 3, the polarization is expressed in terms of E_a as

$$P = \varepsilon_0\chi_e\left(1 - \frac{N\alpha}{3\varepsilon_0}\right)E_a\ . \tag{8}$$

By a direct comparison of Eqs. 5 and 8, after some algebraic operations, we arrive at the well-known Clausius–Mossotti equation,

$$\alpha = \frac{3\varepsilon_0}{N}\left(\frac{\varepsilon_r - 1}{\varepsilon_r + 2}\right). \tag{9}$$

Furthermore, when the magnetic effect is neglected, ε_r is equal to n^2, and Eq. 9 is written as

$$\alpha = \frac{3\varepsilon_0}{\tilde{N}}\left(\frac{n^2 - 1}{n^2 + 2}\right). \tag{10}$$

Equation 10 is called the Lorentz–Lorenz equation in optics.

For anisotropic materials consisting of identical but nonspherical molecules (such as carbon dioxide), the polarizability and electric susceptibility are no longer scalar quantities but second-rank tensors, which we shall denote by $\underline{\underline{\alpha}}$ and $\underline{\underline{\chi_e}}$. Accordingly, the expression for $\boldsymbol{P}$, corresponding to Eq. 3, is written as

$$P = \varepsilon_0\underline{\underline{\chi_e}} \cdot E. \tag{11}$$

Furthermore, the equation corresponding to Eq. 4 is given by

$$p_i = \underline{\underline{\alpha_i}} \cdot E_a. \tag{12}$$

Because we are dealing with identical but nonspherical molecules, the polarizability tensor of each molecule with respect to a fixed frame of reference will be, in general, different than those of other molecules, depending on its orientation in space. Moreover, in this material, p_i would, in general, not lie in the same direction as E_a. Because both p_i and $\underline{\underline{\alpha_i}}$ are different for various molecules, it seems to be reasonable to use an averaged quantity for each of them. Taking a summation of Eq. 12 over all the molecules in V and dividing by N, we obtain

$$p = \underline{\underline{\alpha}}\ \cdot E_a, \tag{13}$$

where we have introduced the averaged quantities with $p \equiv \sum_{i=1}^{N} p_i \Big/ N$ and $\underline{\underline{\alpha}} \equiv \sum_{i=1}^{N} \alpha_i \Big/ N$.

Using Eq. 13, the polarization is written as

$$P = \frac{\sum_{i=1}^{N} p_i}{V} = \frac{Np}{V} = \tilde{N}p = \tilde{N}\underline{\underline{\alpha}} \cdot E_a. \tag{14}$$

Therefore, the electric field induced by the dipoles is

$$E_d = -\frac{P}{3\varepsilon_0} = -\frac{\tilde{N}}{3\varepsilon_0}\underline{\underline{\alpha}} \cdot E_a. \tag{15}$$

The local electric field E is then

$$E = E_a + E_d = \left(\underline{\underline{I}} - \frac{\tilde{N}}{3\varepsilon_0}\underline{\underline{\alpha}}\right) \cdot E_a, \tag{16}$$

where $\underline{\underline{I}}$ is the second-rank unit tensor. Putting Eq. 16 into Eq. 11, the polarization is found to be

$$P = \varepsilon_0\underline{\underline{\chi_e}} \cdot \left(\underline{\underline{I}} - \frac{\tilde{N}}{3\varepsilon_0}\underline{\underline{\alpha}}\right) \cdot E_a. \tag{17}$$

Eliminating $\boldsymbol{P}$ from Eqs. 14 and 17, we arrive at

$$\left[\tilde{N}\underline{\underline{\alpha}} - \varepsilon_0\underline{\underline{\chi_e}} \cdot \left(\underline{\underline{I}} - \frac{\tilde{N}}{3\varepsilon_0}\underline{\underline{\alpha}}\right)\right] \cdot E_a = 0. \tag{18}$$

Because E_a is arbitrary, the term within the square brackets must vanish. After some manipulation, we finally arrive at

the following relationship between the polarizability and susceptibility tensors for anisotropic materials:

$$\underline{\underline{\alpha}} = \frac{3\varepsilon_0}{\tilde{N}}\left(\underline{\underline{\chi_e}} + 3\underline{\underline{I}}\right)^{-1} \cdot \underline{\underline{\chi_e}} = \frac{3\varepsilon_0}{\tilde{N}}\left(\underline{\underline{\varepsilon_r}} + 2\underline{\underline{I}}\right)^{-1} \cdot \left(\underline{\underline{\varepsilon_r}} - \underline{\underline{I}}\right). \tag{19}$$

To obtain this expression, we used the tensorial equation $\underline{\underline{\chi_e}} = \underline{\underline{\varepsilon_r}} - \underline{\underline{I}}$. Equation 19 is the generalized Clausius–Mossotti (tensorial) formula of linear dielectric materials. If we put $\underline{\underline{\varepsilon_r}} = \underline{\underline{n}} \cdot \underline{\underline{n}}$ in Eq. 19 in the absence of a magnetic effect, we obtain the generalized form of the Lorentz–Lorenz equation in optics,

$$\underline{\underline{\alpha}} = \frac{3\varepsilon_0}{\tilde{N}}\left(\underline{\underline{n}} \cdot \underline{\underline{n}} + 2\underline{\underline{I}}\right)^{-1} \cdot \left(\underline{\underline{n}} \cdot \underline{\underline{n}} - \underline{\underline{I}}\right). \tag{20}$$

Equation 20 is used in calculating the birefringence tensor in this study. Again, Eq. 19 was presented (without a derivation) in the article by Mavrantzas and Theodorou (2000a).

A local coordinate transformation used in calculating the polarizability tensor

To calculate the polarizability tensor of the molecules by summing each contribution of the bonds, it is convenient to choose a local Cartesian coordinate system (represented by lowercase letters) attached to each bond (Bower 2002). As shown in Fig. 1, the *X*- and *Y*-axes in the laboratory frame of reference (represented by uppercase letters) are chosen to be the flow and the velocity gradient directions, respectively, and the *Z*-axis is the neutral direction. In the local coordinate system, the *x*-axis is located along the bond direction, the *y*-axis is perpendicular to the *x*-axis and lying in the *X*–*Y* plane, and the *z*-axis (orthogonal to both the *x*- and *y*-axes) is determined by taking the cross product of the *x*- and *y*-axes.

Using these reference frames, we need to find the orthogonal transformation matrix between the laboratory and the local coordinate systems. First, the unit vector in the *x*-direction, denoted by $\hat{x}$, is expressed in terms of the unit vectors $(\hat{X}, \hat{Y}, \hat{Z})$ in the laboratory coordinate system:

$$\hat{x} = \cos\theta\hat{X} + \sin\theta\cos\phi\hat{Y} + \sin\theta\sin\phi\hat{Z}. \tag{21}$$

Next, because $2\hat{y}$ is lying in the *X*–*Y* plane, it can be expressed as

$$\hat{y} = a\hat{X} + b\hat{Y}\,. \tag{22}$$

Using its orthogonal relationship with $\hat{x}$ and the unit length of its magnitude, a and b are

$$a = \mp\sin\phi; b = \pm\cos\phi. \tag{23}$$

Let us choose $a = -\sin\phi$ and $b = \cos\phi$. $\hat{z}$ is then determined as

$$\hat{z} = \hat{x} \times \hat{y} = -\cos\theta\cos\phi\hat{X} - \cos\theta\sin\phi\hat{Y} + \sin\theta\hat{Z} \tag{24}$$

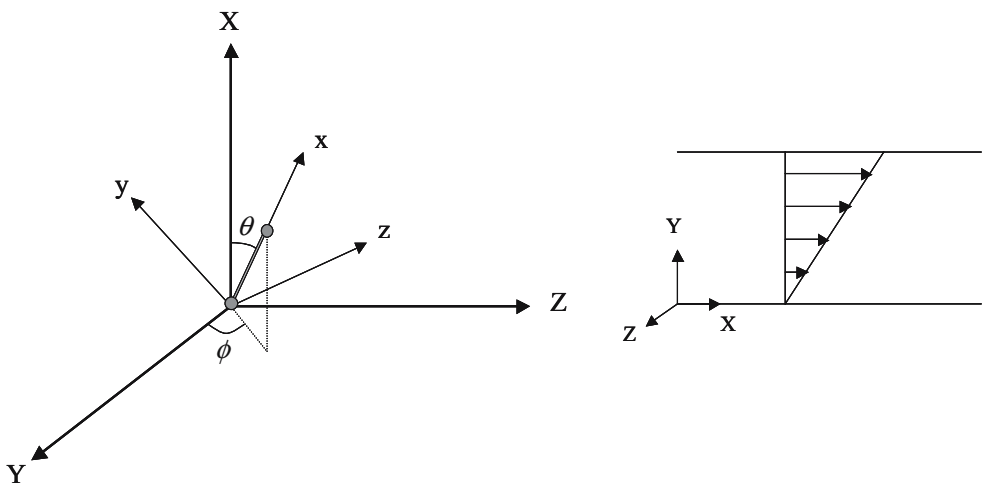

Fig. 1 Schematic diagram (*left*) of the laboratory coordinate system (represented by *XYZ*) and the local coordinate system (represented by *xyz*) attached to a bond. The *x*-direction is located along the bond. The *arrows in the picture* (*right*) represent the velocity field, which is non-zero only in the *X*-direction. The velocity gradient and neutral directions are the *Y*- and *Z*-directions, respectively

The transformation between the two coordinate systems is thus expressed in matrix form as

$$\begin{bmatrix} \hat{x} \\ \hat{y} \\ \hat{z} \end{bmatrix} = \mathbf{M} \cdot \begin{bmatrix} \hat{X} \\ \hat{Y} \\ \hat{Z} \end{bmatrix}, \tag{25}$$

where

$$\mathbf{M} = \begin{bmatrix} \cos\theta & \sin\theta\cos\phi & \sin\theta\sin\phi \\ 0 & -\sin\phi & \cos\phi \\ \sin\theta & -\cos\theta\cos\phi & -\cos\theta\sin\phi \end{bmatrix}. \tag{26}$$

Denoting the longitudinal (x-direction) and transverse (y- and z-direction) polarizabilities of a bond by α_p and α_t, respectively, the polarizability tensor of each bond is in diagonal form in the local coordinate system:

$$(\alpha)_{xyz} = \begin{bmatrix} \alpha_p & 0 & 0 \\ 0 & \alpha_t & 0 \\ 0 & 0 & \alpha_t \end{bmatrix}. \tag{27}$$

Therefore, the polarizability tensor in the laboratory coordinate system is

$$(\alpha)_{XYZ} = \mathbf{M}^T \cdot (\alpha)_{xyz} \cdot \mathbf{M} = \begin{bmatrix} (\cos^2\theta)\alpha_p + (\sin^2\theta)\alpha_t & (\sin\theta\cos\theta\cos\phi)(\alpha_p - \alpha_t) & (\sin\theta\cos\theta\sin\phi)(\alpha_p - \alpha_t) \\ (\sin\theta\cos\theta\cos\phi)(\alpha_p - \alpha_t) & (\sin^2\theta\cos^2\phi)\alpha_p + (\sin^2\phi + \cos^2\theta\cos^2\phi)\alpha_t & (\sin^2\theta\sin\phi\cos\phi)(\alpha_p - \alpha_t) \\ (\sin\theta\cos\theta\sin\phi)(\alpha_p - \alpha_t) & (\sin^2\theta\sin\phi\cos\phi)(\alpha_p - \alpha_t) & (\sin^2\theta\sin^2\phi)\alpha_p + (\cos^2\phi + \cos^2\theta\sin^2\phi)\alpha_t \end{bmatrix}. \tag{28}$$

Before we discuss the simulation methodology, we would like to point out that we have chosen to neglect the C−H bond altogether in calculating the birefringence tensor in this work. We did this because the potential model used herein (described in the next section) to model the linear polyethylene melt is a united-atom model, which treats groups of atoms (in this case, CH_2 and CH_3 groups). Although some scholars (Gao and Weiner 1994; Mavrantzas and Theodorou 2000a) have included the C−H bonds in their calculation of the birefringence by assuming the trans-state of these bonds along the chain backbone, such treatments are still approximate and perhaps inconsistent with the united-atom model. Therefore, to maintain the consistency with the potential model employed in the simulations, we have decided to ignore C−H bonds and only consider C−C bonds in this work. This choice is not considered to be overly restrictive because all the properties can be still calculated without any corrections, except the absolute value of the stress–optical coefficient C. In other words, the only weak point because of the neglect of C−H bonds lies in obtaining a quantitative estimate of C. In this regard, we should also note that there does not even seem to exist as yet universally accepted values of the experimental bond polarizabilities for C−C and C−H bonds (Treloar 1975). Therefore, our choice is reasonable, as it does not affect the main purpose of this study and substantially reduces the computational cost of the simulation (by not including every atom explicitly). The bond polarizabilities of the C−C bond employed in this work were obtained from Table 9.5 of Bower (2002): $\alpha_p = 10.8 \times 10^{-41}$ and $\alpha_t = 2.8 \times 10^{-41}$ F m^2.

Simulation methodology

Equations of motion

The melt studied in this work is $C_{50}H_{102}$, which is sufficient in length to see the flow effect on birefringence and, at the same time, computationally feasible across a broad range of shear rates. With this melt, we have performed *NVT* canonical nonequilibrium molecular dynamics (NEMD) simulations using the SLLOD equations of motion for a homogeneous shear flow (Evans and Morriss 1990). To maintain a constant temperature, we employed the Nosé–Hoover thermostat (Nosé 1984a, b; Hoover 1985). The equations of motion are given by

$$\begin{aligned} \dot{q}_{ia} &= \frac{p_{ia}}{m_{ia}} + q_{ia} \cdot \nabla v, \\ \dot{p}_{ia} &= F_{ia} - p_{ia} \cdot \nabla v - \frac{p_\varsigma}{Q} p_{ia}, \\ \dot{\varsigma} &= \frac{p_\varsigma}{Q}, \\ \dot{p}_\varsigma &= \sum_i \sum_a \frac{p_{ia}^2}{m_{ia}} - DNk_BT, \end{aligned} \tag{29}$$

where subscripts i and a are used as indices of molecular and atomic number, respectively. The quantities p_{ia} and q_{ia}, respectively, denote the momentum and position vectors of

atom a in molecule i. F_{ia} is the force on atom a in molecule i of mass m_{ia}. D represents dimensionality, V the system volume, N the total number of atoms, T the absolute temperature, and k_B the Boltzmann constant. ς and p_ς, respectively, are the coordinate- and momentum-like variables of the Nosé–Hoover thermostat, and Q ($=DNk_BT\tau^2$) is the mass parameter of the thermostat. (τ is the characteristic frequency of the thermostat.) In shear flow,

$$\nabla v = \begin{bmatrix} 0 & 0 & 0 \\ \dot{\gamma} & 0 & 0 \\ 0 & 0 & 0 \end{bmatrix}, \tag{30}$$

where $\dot{\gamma}$ is the applied shear rate. The equations of motion were numerically integrated using a modified version (including the velocity field terms [Cui et al. 1996a]) of the reversible reference system propagator algorithm (r-RESPA), originally developed by Tuckerman et al. (1992).

Potential model

We employed the well-known Siepmann–Karaborni–Smit united-atom model developed by Siepmann et al. (1993) for the bond-bending, bond-torsional, and interatomic interactions, but replaced the rigid bond by a flexible one for the bond-stretching interaction. This potential model has been successfully applied in NEMD simulations of various chain lengths of polyethylene melts under shear (Cui et al. 1996b) and planar elongation flow (Baig et al. 2005, 2006).

To avoid unnecessary repetition, we briefly present the main features of the potential model. The bond-stretching, bond-bending, bond-torsional, and interatomic Lennard–Jones (LJ) interactions, respectively, are given by

$$V_{str}(l) = \frac{1}{2}k_{str}\left(l - l_{eq}\right)^2, \tag{31}$$

$$V_{ben}(\theta) = \frac{1}{2}k_{ben}\left(\theta - \theta_{eq}\right)^2, \tag{32}$$

$$V_{tor}(\phi) = \sum_{m-0}^{3} a_m(\cos\phi)^m, \tag{33}$$

and

$$V_{LJ}(r) = 4\varepsilon_{ab}\left[\left(\frac{\sigma_{ab}}{r}\right)^{12} - \left(\frac{\sigma_{ab}}{r}\right)^{6}\right]. \tag{34}$$

The parameter ratios k_{str}/k_B and k_{ben}/k_B are equal to 452,900 K/Å^2 and 62,500 K/rad^2, respectively, and a_0/k_B= 1,010, a_1/k_B=2,019, a_2/k_B=136.4, and a_3/k_B=−3,165 K. The equilibrium bond distance is l_{eq}=1.54 Å, and the equilibrium bond angle is θ_{eq}=114°. For the LJ interactions between different atoms (say, a and b), the Lorentz–Berthelot mixing rule was employed as $\varepsilon_{ab}=(\varepsilon_a\varepsilon_b)^{1/2}$ and $\sigma_{ab}=(\sigma_a+\sigma_b)/2$, with the energy and size parameters ε/k_B and σ being 47 K and 3.93 Å for the CH_2 united-atom and 114 K and 3.93 Å for the CH_3. The cutoff distance of the LJ interactions used in this work was $2.5\sigma_{CH2}$.

Simulation conditions

We employed 120 molecules of $C_{50}H_{102}$ in a rectangular box, enlarged in the X-direction, with dimensions ($X\times Y\times Z$) of 93×45×45 Å^3. The X-dimension was chosen to be sufficiently large to avoid any undesirable system-size effects at high shear rates where chains are quite extended and oriented in the flow direction. The temperature and density were chosen as 450 K and 0.7438 g/cm^3. We used 18 different shear rates covering a large range of dimensionless shear rates, $\dot{\gamma}\left(m\sigma^2/\varepsilon\right)^{1/2} = 0.0005 - 1.0$ in reduced units (this corresponds to $\dot{\gamma} = 2.1\times10^7 - 4.3\times10^{11}$ s^{-1} in real units).

The lowest value of the shear rate is regarded as very small (although still high in practical experiments) in typical NEMD simulations, considering that the longest relaxation time (the so-called Rouse time) of the system λ was equal to 500 ps (Baig et al. 2006). Consequently, the inverse of λ (regarded as an approximate critical shear rate for the onset of shear-thinning behavior) is 0.0047 in reduced units, below which a large effect of Brownian motion of particles makes it difficult to measure the response of system to the flow field. (This will be discussed in more detail later in "Results and discussion".) Furthermore, it usually takes a much longer simulation time to reach a steady state as shear rate decreases. Despite these difficulties, we chose such low strain rates to observe in more detail the linear stress–optical behavior over a wide range of shear rates. Therefore, to obtain statistically reliable results for low shear rates, we performed very long simulations, i.e., 70 ns at the lowest shear rate. In applying the r-RESPA integrator, two different time steps were used: the large time step of 2.35 fs was employed for intermolecular LJ interactions and the small time step of 0.235 fs for the bond-stretching, bond-bending, bond-torsional, and intramolecular LJ interactions.

Results and discussion

There are only four nonzero independent components of the stress tensor σ in simple shear flow, as represented by Eq. 30: these are σ_{xx}, σ_{yy}, σ_{zz}, and σ_{xy} (Morrison 2001). This situation also applies to the other tensors examined in this

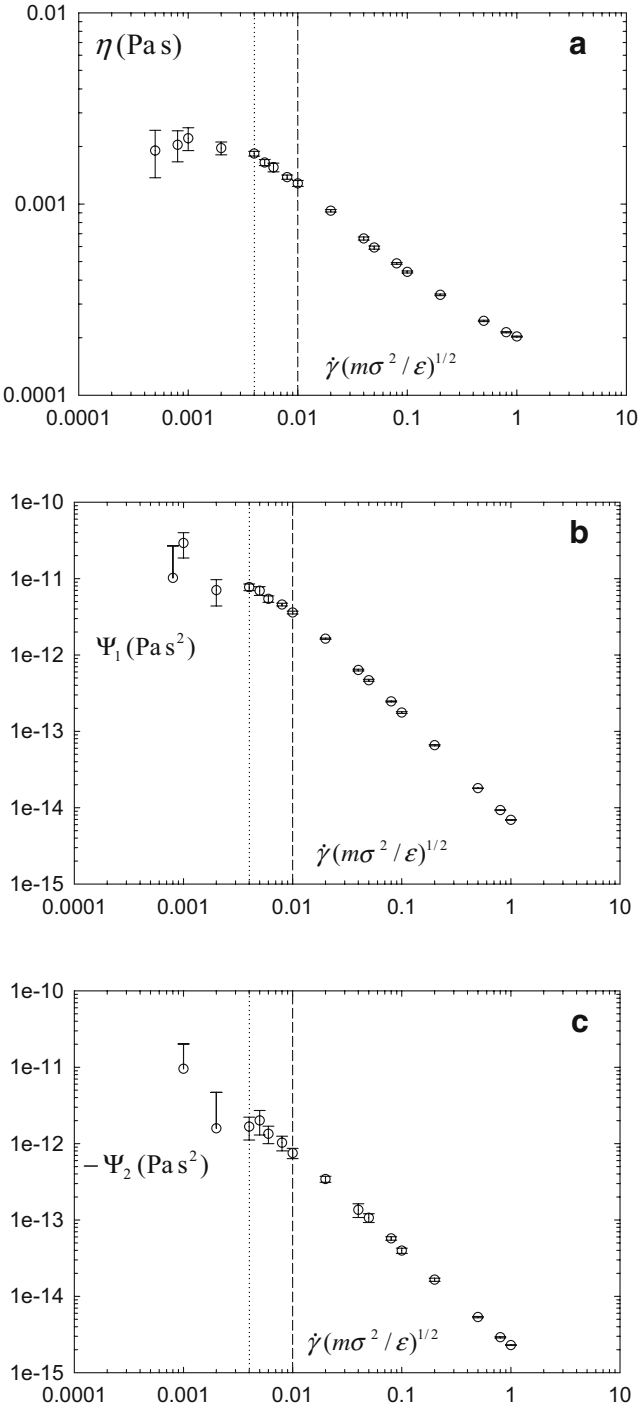

Fig. 2 Plots of the steady-state material functions vs shear rate: **a** shear viscosity η, **b** the first normal stress coefficient Ψ_1, and **c** the second normal stress coefficient Ψ_2

article, namely, the conformation tensor $\tilde{c}$, the orientational tensor u, and the birefringence tensor n. Furthermore, experimentally, we can only measure the difference between the normal (or diagonal) components of the stress tensor but not their absolute values (Bird et al. 1987). Therefore, in simple shear flow, we consider only three independent measurable physical quantities (or "characteristic functions") of the stress tensor (and the other tensors, $\tilde{c}$, u, and n, as well): $\sigma_{xx}-\sigma_{yy}$, $\sigma_{yy}-\sigma_{zz}$, and σ_{xy}. The corresponding three steady-state material functions in simple shear flow are defined as

$$\eta \equiv \sigma_{xy}\Big/\dot{\gamma};\ \Psi_1 \equiv -\left(\sigma_{xx}-\sigma_{yy}\right)\Big/\dot{\gamma}^2;\ \Psi_2 \equiv -\left(\sigma_{yy}-\sigma_{zz}\right)\Big/\dot{\gamma}^2. \tag{35}$$

First, we examine the three material functions, which are displayed in Fig. 2. Consistent with many existing experimental results (Morrison 2001; Bird et al. 1987), all three properties show shear-thinning behavior with increasing shear rate, after a plateau in the linear regime at low shear rates. The dotted line vertically drawn at the reduced shear rate of 0.004 in each part of the figure represents the boundary between the linear and nonlinear regimes. This value of the shear rate appears to agree well with the theoretically predicted one $\left(\dot{\gamma}=1/\lambda\right)$ at which the Weissenberg number $\left(We=\lambda\dot{\gamma}\right)$ is equal to unity and nonlinear characteristics of material properties begin to appear. This trend has been observed for many polymeric systems—see, for example, Chapter 2 of Bird et al. (1987). One method to find the characteristic time λ is to observe the time correlation function of the end-to-end chain vector, by means of which we have determined λ=500 ps (Baig et al. 2006). Using the calculated value of λ, the critical shear rate for shear-thinning turns out to be 0.0047 in reduced units $\left(\dot{\gamma}(m\sigma^2/\varepsilon)^{1/2}\right)$, which is very close to the boundary value of $\dot{\gamma}\left(m\sigma^2/\varepsilon\right)^{1/2}=0.004$ directly obtained from the material functions. The other vertical line (represented by the dashed line) drawn at $\dot{\gamma}\left(m\sigma^2/\varepsilon\right)^{1/2}=0.01$ indicates an approximate boundary between the linear and nonlinear stress–optical behavior between the stress and birefringence tensors. That is, it turns out that the linear SOR appears to be valid up to $\dot{\gamma}\left(m\sigma^2/\varepsilon\right)^{1/2}=0.01$, after which, it appears to fail, as shown in Fig. 8. (This behavior will be considered in detail later.) Therefore, we inserted these vertical lines in most of the figures presented in this

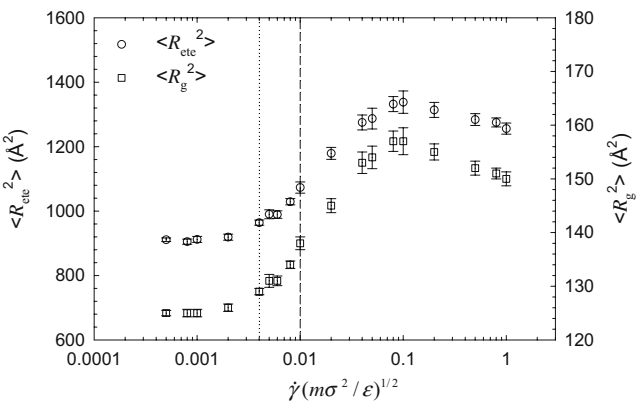

Fig. 3 Plots of the mean square chain end-to-end distance and the mean square chain radius of gyration with respect to shear rate

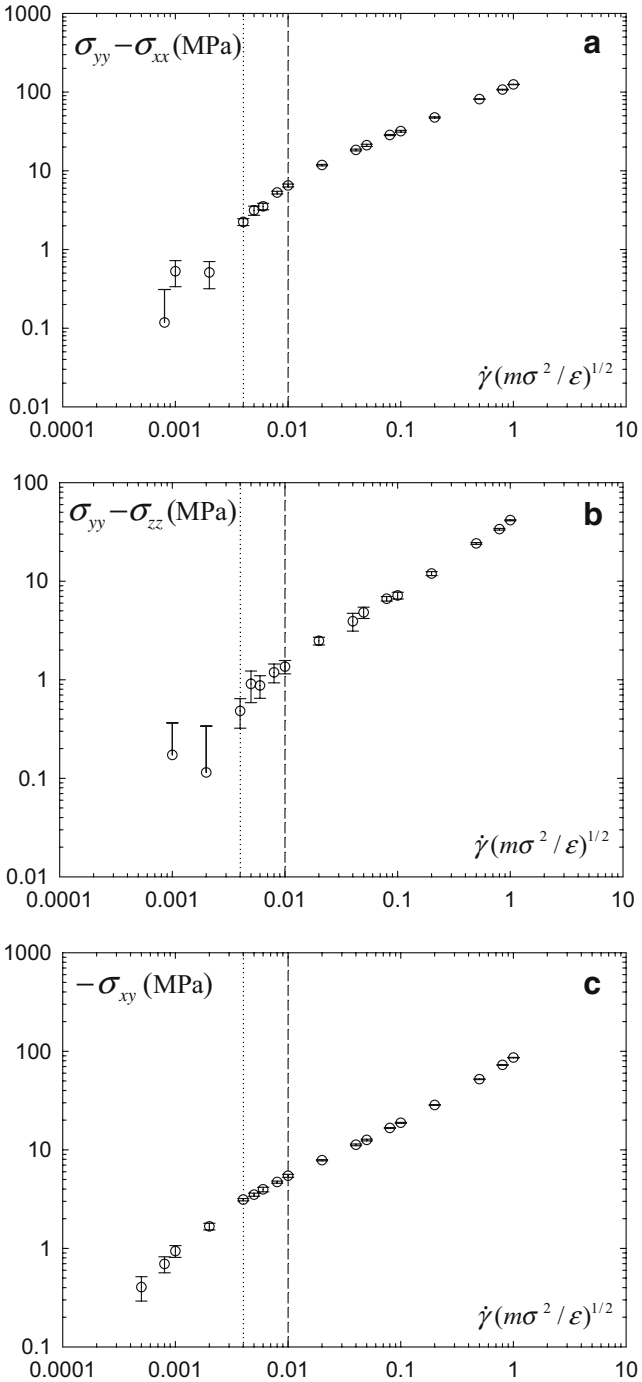

Fig. 4 Plots of the three independent properties of the stress tensor σ as functions of shear rate: **a** σ_{xx}–σ_{yy}, **b** σ_{yy}–σ_{zz}, and **c** σ_{xy}

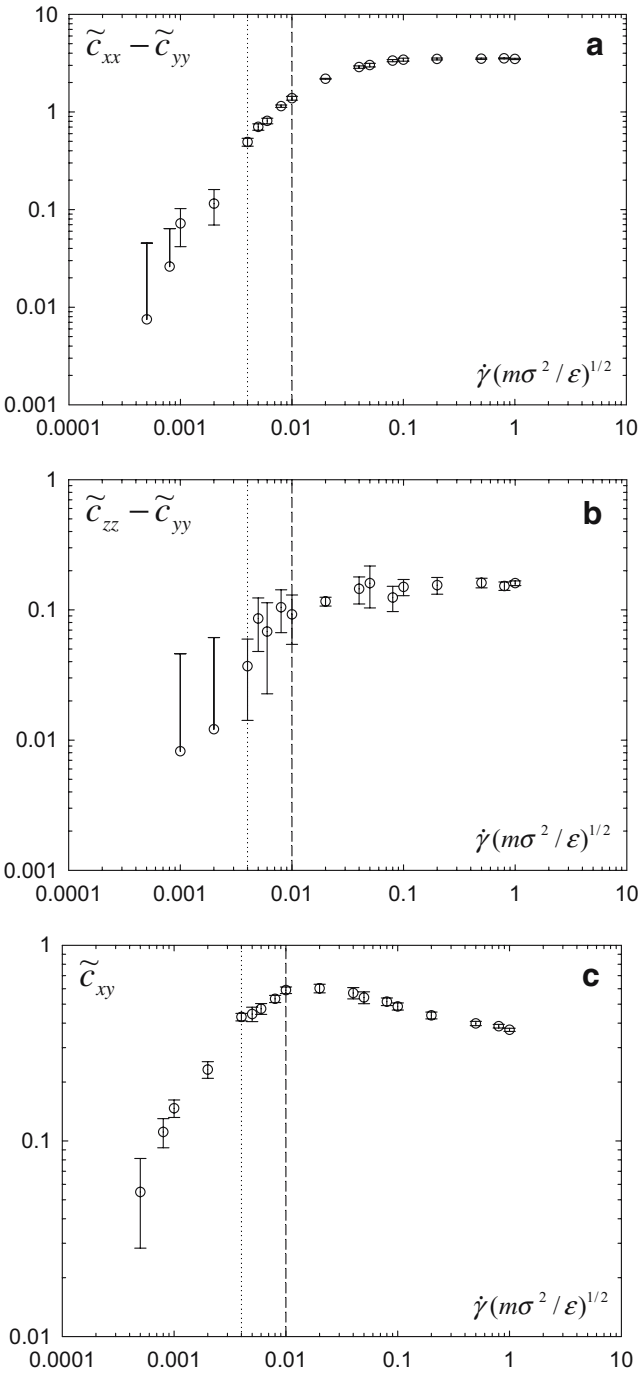

Fig. 5 The same as Fig. 4 for the conformation tensor

manuscript for a clear understanding where each data point lies (i.e., whether it lies in the linear or nonlinear regimes with respect to shear-thinning or the SOR).

In Fig. 3, we present two important structural quantities, the mean square chain end-to-end distance and the mean square chain radius of gyration, denoted by $\langle R^2_{\mathrm{ete}}\rangle$ and $\langle R^2_{\mathrm{g}}\rangle$, respectively. As shear rate increases, the chains become more and more aligned in the flow direction with an anisotropically elongated shape. This results in the increase in both $\langle R^2_{\mathrm{ete}}\rangle$ and $\langle R^2_{\mathrm{g}}\rangle$ with shear rate, as shown in the figure. However, at high shear rates, i.e., $\dot{\gamma}(m\sigma^2/\varepsilon)^{1/2} > 0.1$, both quantities appear to decrease with shear rate. A similar behavior has also been observed by Cui et al. (1996b) in their study using the short alkane chains $C_{10}H_{22}$, $C_{16}H_{34}$, and $C_{24}H_{50}$ under shear. This phenomenon can be explained in a dynamic sense, adopting a mean-field concept of restricting the chain dimensions at

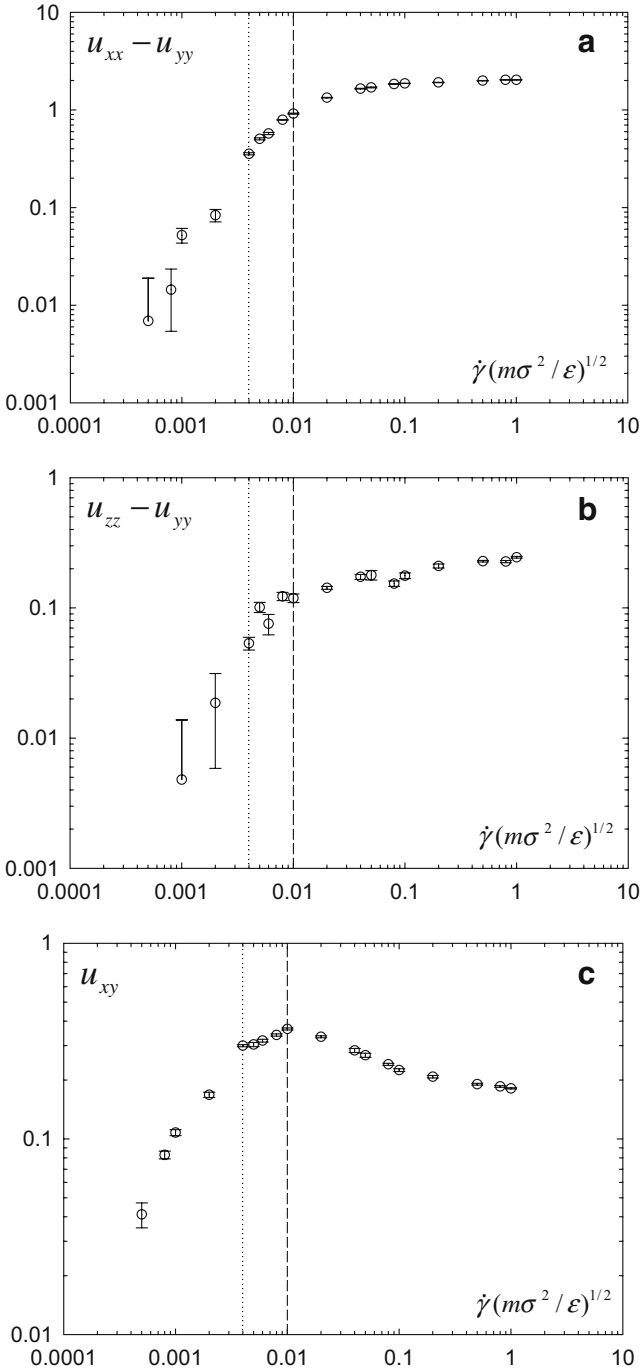

Fig. 6 The same as Fig. 4 for the orientational tensor u

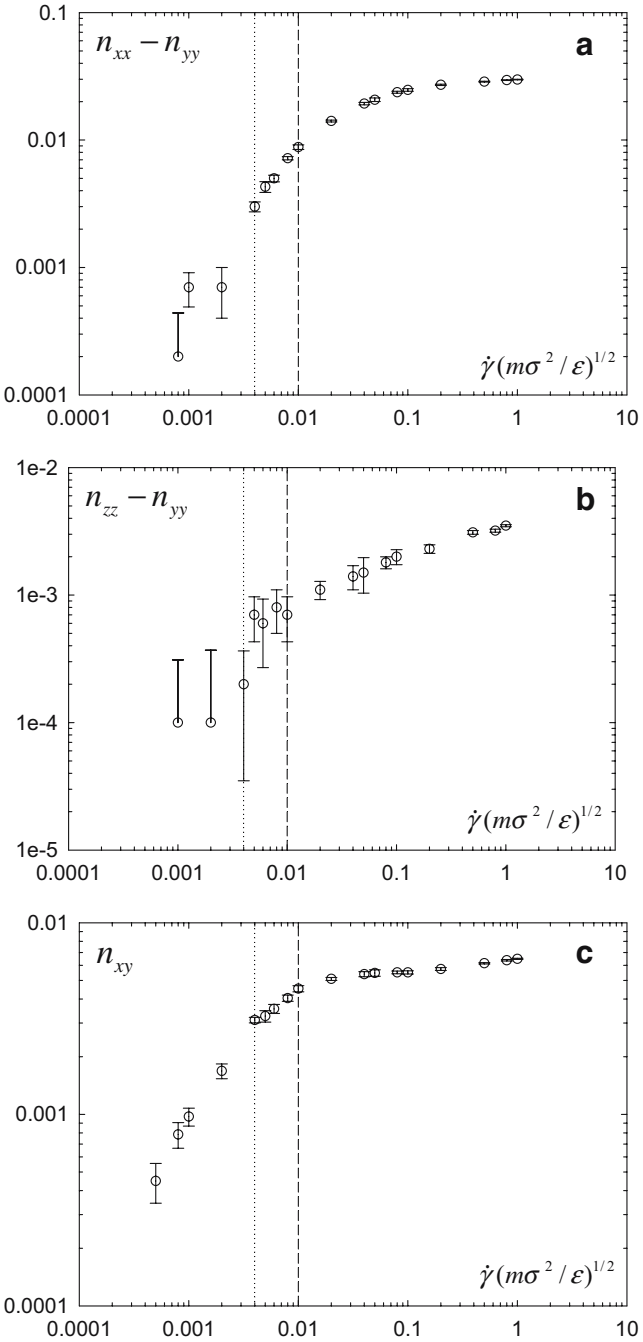

Fig. 7 The same as Fig. 4 for the birefringence tensor n

high strain rates because of a large number of molecular collisions between atoms, which was originally proposed by Moore et al. (2000) and discussed by Baig et al. (2005). (Readers who are interested in the details on this issue are referred to these papers.)

Another interesting point is to compare the values of $\langle R^2_{\mathrm{ete}} \rangle$ shown in Fig. 3 and that of the fully extended chain with the equilibrium bond length and angle in the all-trans state. $\langle R^2_{\mathrm{ete}} \rangle$ of the fully stretched chain is calculated as 4,007 Å^2. Thus, even the highest value, $\langle R^2_{\mathrm{ete}} \rangle$=1,338 Å^2 observed at $\dot{\gamma}(m\sigma^2/\varepsilon)^{1/2} = 0.1$, is found to be only about one third of that at the fully stretched state. Therefore, chains do not reach their maximum extensions in shear flow. This is interesting because (as mentioned earlier) the SOR has been customarily thought to become invalid because of the saturation of chain extension and orientation (Janeschitz-Kriegl 1983; Treloar 1975). However, as indicated by the dashed line in the figure and directly shown in

Fig. 8, the failure of the SOR begins at a fairly low strain rate without even being close to the maximum chain extension.

Figures 4, 5, 6, and 7 show the three independent properties (*xx–yy*, *yy–zz*, and *xy* components) of the stress, conformation, orientation, and birefringence tensors, in that order, as functions of shear rate. In conjunction with the material functions shown in Fig. 2, the two normal stress differences and the shear stress shown in Fig. 4 appear to increase monotonically with increasing shear rate, which is consistent physically. However, the degree of increase for each property is observed to vary with shear rate, as revealed by its degree of shear-thinning behavior in Fig. 2. Notice that the *yy–zz* component of stress is shown to be statistically less reliable, compared with the *xx–yy* and *xy* quantities. (In fact, as will be shown below, this is also true for the other second-rank tensors.) Keeping this behavior in mind, we examine the variation of the conformation tensor with respect to shear rate, which is shown in Fig. 5. Initially, all three quantities appear to increase with increasing shear rate. At high shear rates, however, both $\tilde{c}_{xx} - \tilde{c}_{yy}$ and $\tilde{c}_{yy} - \tilde{c}_{zz}$ do not increase any further but reach asymptotic values. Furthermore, $\tilde{c}_{xy}$ is observed to reach the maximum point around $\dot{\gamma}\left(m\sigma^2/\varepsilon\right)^{1/2} = 0.01 - 0.02$ (which approximately coincides with the critical shear rate of the SOR) and then decreases with increasing shear rate. From the quantitative analysis of the results, this seems to occur mainly because of the relatively larger decrease in $\tilde{c}_{yy}$ than the increase in $\tilde{c}_{xx}$ above the critical shear rate. (However, there seems to be other effects operating as well, such as a nonuniform distribution of the azimuthal angle in *Y–Z* plane.) Comparing with the results of the stress tensor shown in Fig. 4, it is evident that a linear relationship between the stress and conformation tensors can be realized only at low shear rates, and nonlinear behavior occurs at high shear rates (see Fig. 10). Similar phenomena are also observed for the orientational tensor u, which is shown in Fig. 6. This result can be understood through the close relationship between $\tilde{c}$ and u under the (plausible) assumption of a fairly narrow (approximately Gaussian) distribution of the chain end-to-end distance.

We also examined the three components of the birefringence tensor, which were calculated using Eq. 20 and are presented in Fig. 7. All three quantities appear to increase rather quickly with shear rate, up to the critical shear rate around $\dot{\gamma}\left(m\sigma^2/\varepsilon\right)^{1/2} = 0.01$. After that, all of them appear to increase relatively slowly and display asymptotic behavior at high shear rates. This behavior is quite different from that of the other tensors. Considering all the above results for the four tensors, we would not expect a simple linear relationship between any two of them.

The plots of the birefringence vs stress tensor are presented in Fig. 8. Because the *yy–zz* quantity shown in Fig. 8b experiences large fluctuations, we examine only the *xx–yy* and *xy* quantities. It is apparent from the figure that there is a clear, linear relationship between n and σ up to $\dot{\gamma}\left(m\sigma^2/\varepsilon\right)^{1/2} = 0.01$, at which point, the shear stress and the first and second normal stress differences are 5.5±0.2, 6.5±0.3, and 1.4±0.2 MPa, respectively. (Also note that the onset of shear-thinning behavior [represented by dotted line] occurs at $-\sigma_{xy}$=3.2±0.1 MPa, $\sigma_{yy}-\sigma_{xx}$=2.2±0.2 MPa, and $\sigma_{yy}-\sigma_{zz}$=0.5±0.2 MPa.) These results appear to be consistent with the experimental findings for the critical

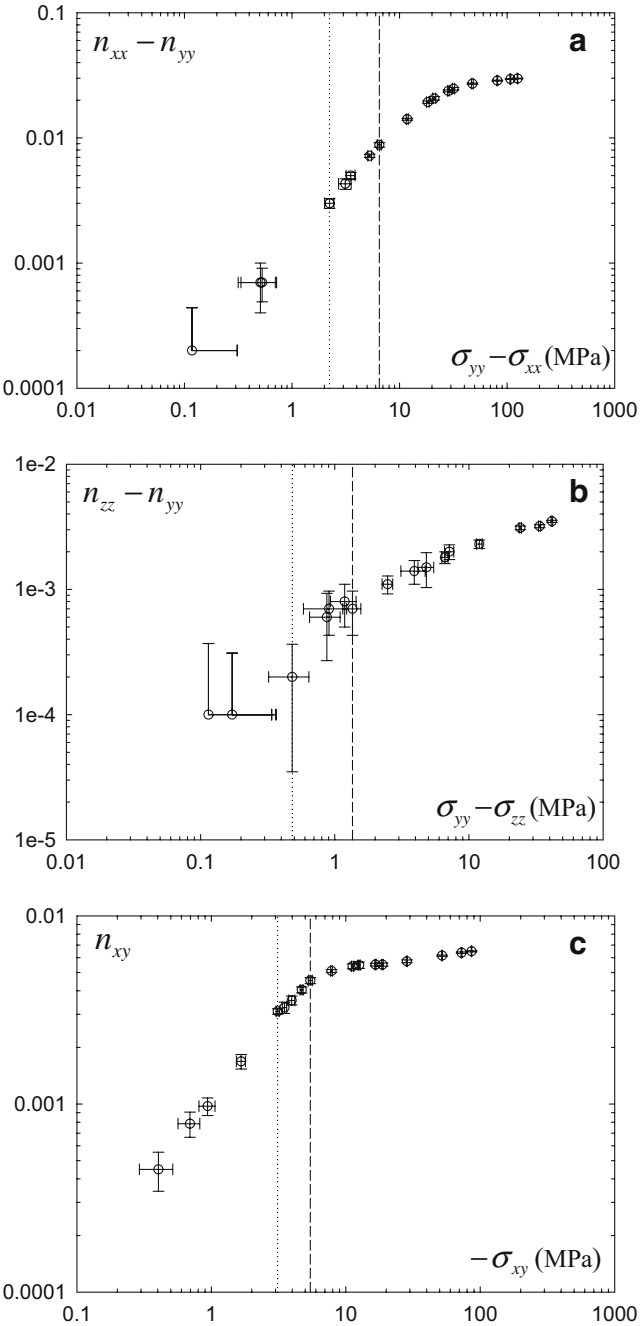

Fig. 8 Comparison of the steady-state values between the birefringence tensor n and the stress tensor σ

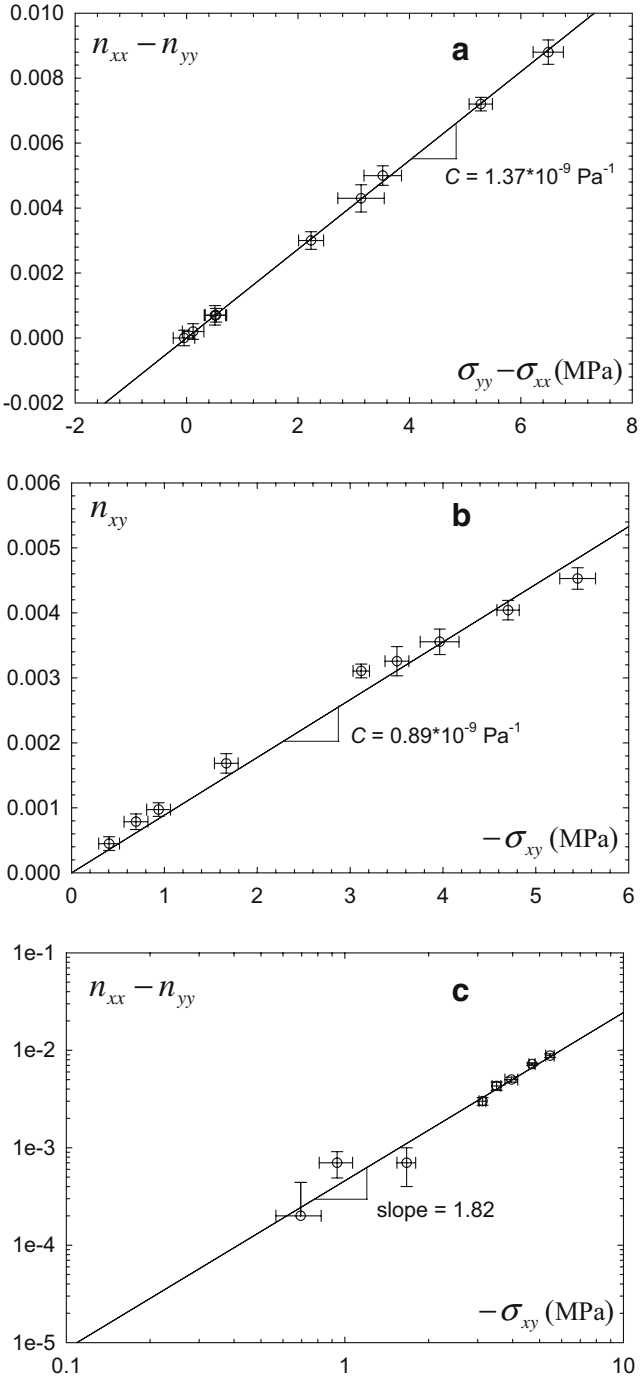

Fig. 9 Linear regression of data of n vs σ at low shear rates where the SOR is valid: **a** and **b** calculate the stress–optical coefficient C based on n_{xx}–n_{yy} vs σ_{xx}–σ_{yy} and n_{xy} vs σ_{xy}, respectively, and **c** shows the slope of n_{xx}–n_{yy} vs σ_{xy}. We present the stress optical coefficient as the average value between the two quantities from **a** and **b**. (The value from the yy–zz quantity was not taken into account because of its rather large statistical uncertainty, relative to the others.)

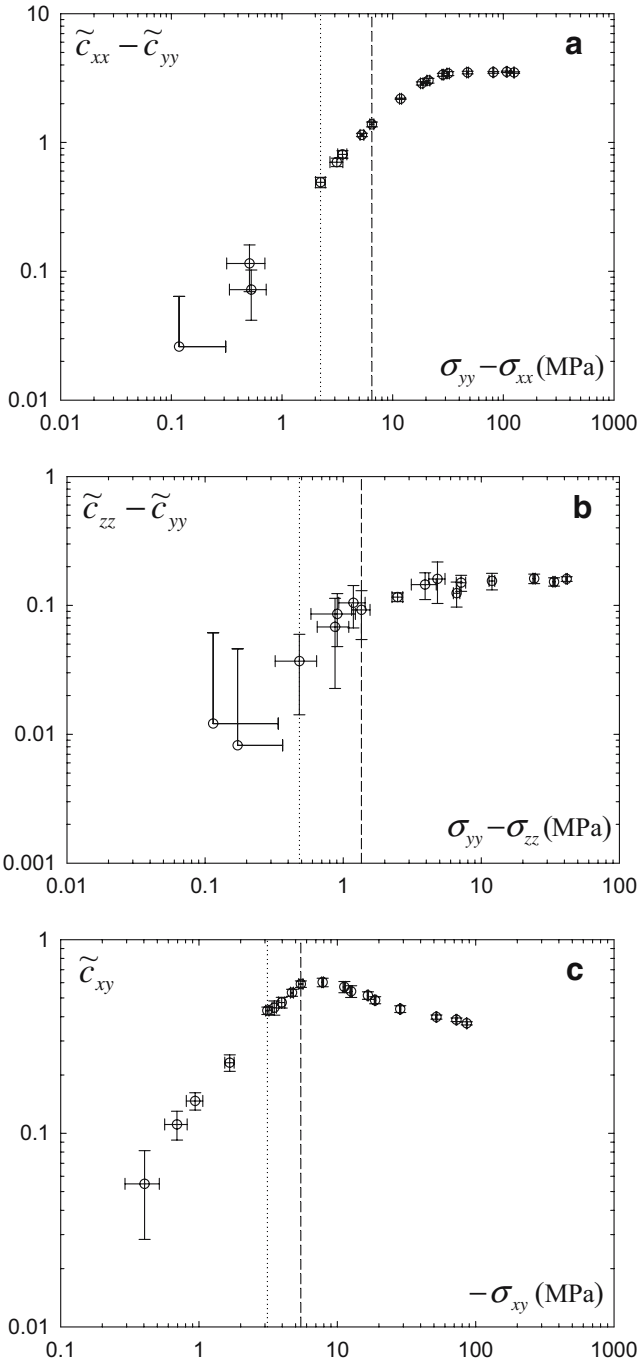

Fig. 10 The same as Fig. 8 for the conformation tensor, $\tilde{c}$, and the stress tensor σ at various shear rates: **a** $\tilde{c}_{xx} - \tilde{c}_{yy}$ vs. $\sigma_{xx} - \sigma_{yy}$, **b** $\tilde{c}_{xy} - \tilde{c}_{zz}$ vs. $\sigma_{yy} - \sigma_{zz}$, and **c** $\tilde{c}_{xy}$ vs. σ_{xy}

tensile stress of the SOR under uniaxial elongation flow being of the order of megapascals (Janeschitz-Kriegl 1983; Luap et al. 2005). As mentioned earlier, considering an experimentally known fact that it is very difficult to find the critical stress of the SOR for polymeric materials for shear flow, the present result of the critical shear stress (≈5.5 MPa) of linear polyethylene melt of $C_{50}H_{102}$ is of potential value from both experimental and theoretical viewpoints.

Using the above results between n and σ, we can extract the stress–optical coefficient C of the present system, for which only data at shear rates of $\dot{\gamma}(m\sigma/\varepsilon)^{1/2} \leq 0.01$ should be used. The results are shown in Fig. 9. As mentioned

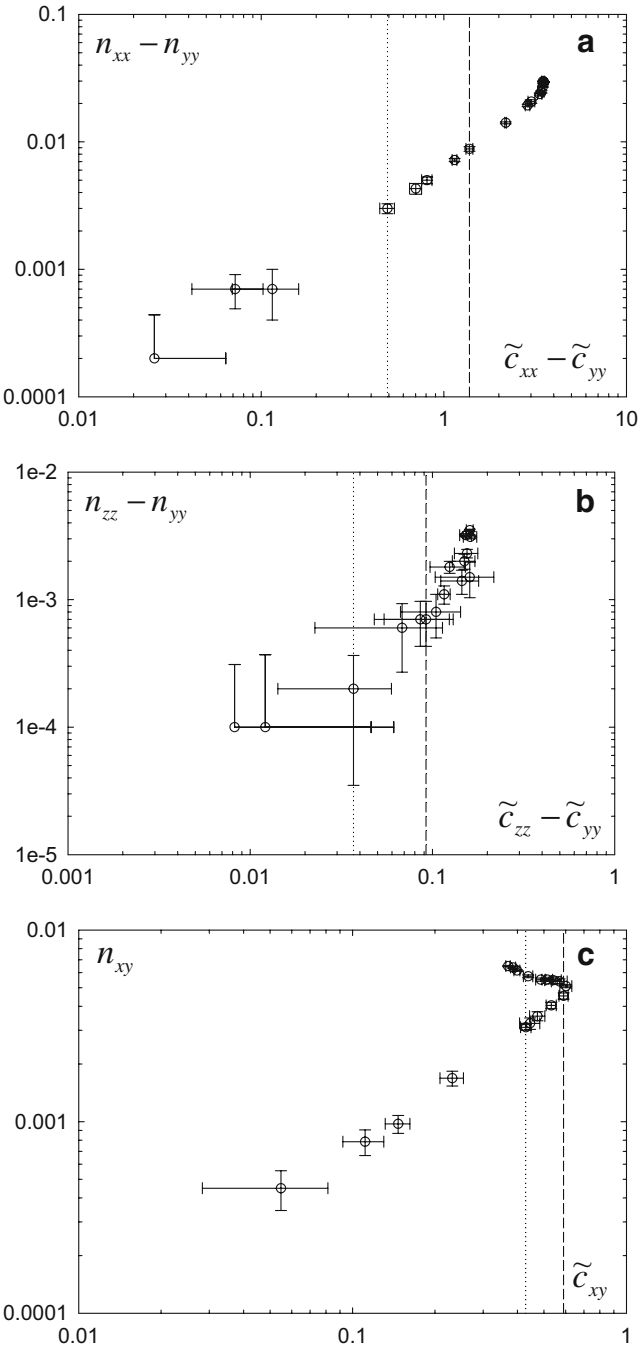

Fig. 11 The same as Fig. 8 for the birefringence tensor n and the conformation tensor $\tilde{c}$

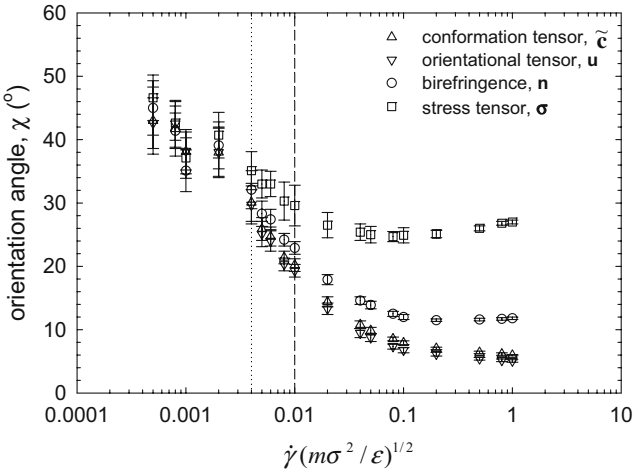

Fig. 12 Comparison of the orientation angle χ as a function of shear rate between , u, n, and σ

above, because of the relatively large uncertainty in the *yy–zz* quantity, we have calculated C using only the *xx–yy* and *xy* quantities. As shown in Fig. 9a and b, the slope is found to be $(1.37\pm0.1)\times10^{-9}$ Pa^{-1} for *xx–yy* and $(0.89\pm0.3)\times10^{-9}$ Pa^{-1} for *xy*. If we average these two values, the stress–optical coefficient C for $C_{50}H_{102}$ at T=450 K and ρ=0.7438 g/cm^3 is estimated as $(1.13\pm0.4)\times10^{-9}$ Pa^{-1}. This value is of the same order of magnitude as the experimentally reported value of 2.35×10^{-9} Pa^{-1} for a high molecular weight, high-density linear polyethylene melt at T=423 K (Janeschitz-Kriegl 1983). As mentioned before, this quantitative difference might be largely due to the neglect of C−H bonds. We also report the slope of n_{yy}–n_{xx} vs $-\sigma_{xy}$ in Fig. 9c. The slope of 1.82±0.2 agrees fairly well with the theoretical value of 2 under the SOR.

Figure 10 shows the change of $\tilde{c}$ with respect to σ. As in Fig. 8 for n vs σ, there appears to be a fairly linear relationship between $\tilde{c}$ and σ in both the *xx–yy* and *xy* quantities up to a shear rate of $\dot{\gamma}(m\sigma^2/\varepsilon)^{1/2} = 0.01$. With a further increase in shear stress, $\tilde{c}_{xx} - \tilde{c}_{yy}$ and $\tilde{c}_{yy} - \tilde{c}_{zz}$ eventually seem to reach certain asymptotic values, and $\tilde{c}_{xy}$ appears to even decrease after passing through a maximum.

In Fig. 11, we make a similar comparison between n and $\tilde{c}$. It might be thought at first that n would be strictly proportional to $\tilde{c}$, regardless of shear rate, because this tensor represents the inherent microstructure of the melt. However, as seen in the figure, such a linear relationship appears to be valid only up to $\dot{\gamma}(m\sigma^2/\varepsilon)^{1/2} = 0.01$, represented by the dashed line. This is particularly clear in Fig. 11c for the *xy* quantity, where a sudden directional change occurs at $\dot{\gamma}(m\sigma^2/\varepsilon)^{1/2} = 0.01$. This result implies a definite difference between the fine-grained property (n) and the coarse-grained property $\left(\tilde{c}\right)$ in the highly nonlinear regime. It is interesting to note the exact match between the critical shear rate of the SOR and that of n vs $\tilde{c}$.

As another important physical property, the orientation angle χ is plotted as a function of shear rate in Fig. 12 for each tensor. The orientation angle has been calculated through the eigenvector analysis: the eigenvector corresponding to the largest eigenvalue of each tensor is the director, and χ is the angle between the director and the flow direction (Allen and Tildesley 1987). As seen in the figure, in general, χ appears to be different for each tensor, except for $\tilde{c}$ and u (thus indicating the narrow Gaussian distribution of the end-to-end distance). In other words, the principal frames of reference are observed to be different

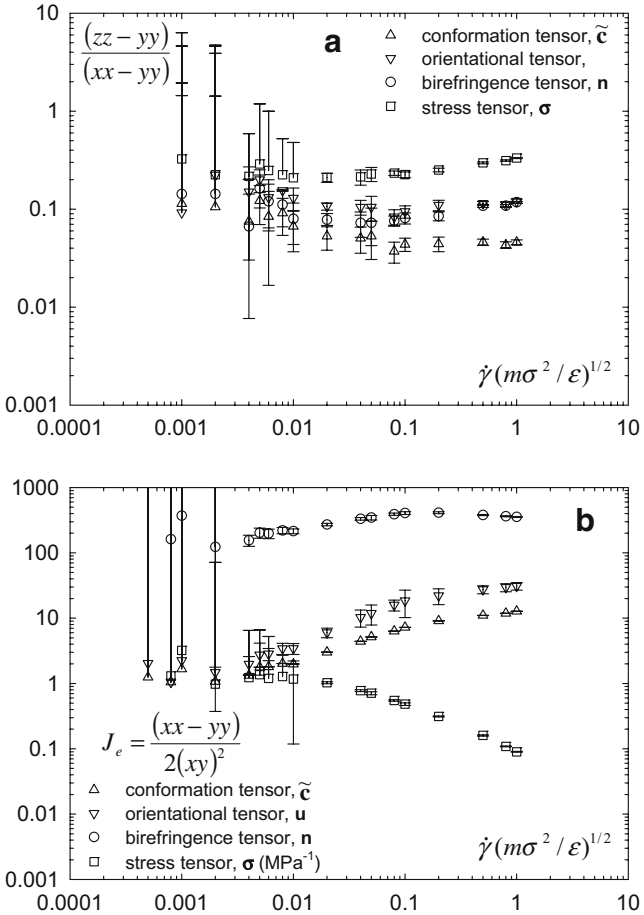

Fig. 13 Plots of **a** $(zz–yy)/(xx–yy)$ and **b** the equilibrium shear compliance as functions of shear rate between $\tilde{c}$, u, n, and σ

between the various tensors. This difference becomes larger with increasing shear rate, in particular, above the critical shear rate of the SOR. While χ (also called the extinction angle) of the birefringence continues to decrease with increasing shear rate and eventually approaches an asymptotic value of about 12° at high shear rates, those of $\tilde{c}$ and u asymptote to smaller values of about 5°. In contrast, χ of the stress tensor initially decreases with increasing shear rate, but appears to pass a minimum value and then increases slightly. Afterwards, for high shear rates, it seems to approach an asymptotic value of 27°, which is quite different than those of other tensors.

Lastly, we plot the ratios among the three independent quantities for each tensor in Fig. 13. As shown in Fig. 13a, the qualitative behavior of the ratio between the $xx–yy$ and $yy–zz$ quantities of each tensor with varying shear rate seems to be similar. However, the quantitative results appear to vary significantly. In Fig. 13b, $J_e = (xx-yy)/\left[2(xy)^2\right]$, which is called the shear compliance for the stress tensor, is plotted as a function of shear rate. J_e appears to be constant at relatively low shear rates but can change dramatically at higher shear rates. More specifically, while J_e of the conformation and orientation tensors appear to increase with shear rate and seem to approach asymptotic values at very high shear rates, J_e of the stress tensor continues to decrease with increasing shear rate. In contrast, J_e of the birefringence appears to pass through a maximum at an intermediate shear rate. The quantitative value of J_e of the stress for this melt is roughly equal to 1.1×10^{-7} Pa^{-1}.

There have recently appeared in the literature some detailed discussions of the effect of the glassy stress on the breakdown of the conventional SOR (Osaki and Inoue 1996; Inoue et al. 1999, 2000). This can be readily understood from a modified equation for the SOR, as described in the above references,

$$\Delta n(t) = C_R \Delta\sigma_R + C_G \Delta\sigma_G. \tag{36}$$

Herein, the subscripts R and G represent the rubbery and the glassy contributions to the stress tensor, respectively. This glassy contribution is, however, expected to be very small in the present polyethylene system for several reasons, as follows.

First, Inoue et al. (1999) investigated four relatively short-chain polystyrene melts in the range of M_w=1,050–10,500g/mol, and in the later dynamic birefringence study (Inoue et al. 2000), only the shortest polystyrene sample with M_w=1,050g/mol was employed. This chain length corresponds to only one Kuhn segment of a polystyrene chain. In contrast, based on the existing experimental results of the mean-squared end-to-end distance, the Kuhn segment of linear polyethylene melts is estimated to contain approximately ten methylene groups (see, for example, Flory 1969). Therefore, each molecule of $C_{50}H_{102}$ employed in the present study would consist of five Kuhn segments, which correspond to polystyrene melts of M_w= 5,250g/mol. In addition, it was reported by Inoue et al. (1999) that polystyrene melts with M_w>5,000g/mol can be well fitted by the multibead-spring (Rouse) model. Furthermore, one must take into account that linear polyethylene chains are much more flexible than polystyrene chains, which supports the notion that the glassy contribution in the present system would be much weaker. Second, as shown by Inoue et al. (1996), for polystyrene melts, the (planar) phenyl side group attached to the main chain backbone apparently magnifies the glassy contribution. Such a side group is entirely absent in linear polyethylene chains. Third, whereas the highest temperature used for the shortest polystyrene melt (M_w=1,050g/mol) in Inoue et al. (2000) was only T_g+30 °C, the temperature imposed in our system was 177 °C (450 K), which is even higher than the melting point of HDPE, T_m=135 °C (≈T_g+300 °C, assuming T_g=−120 °C, as reported in some of the literature). At this very high temperature, the glassy contribution is surely even more negligible.

As a consequence of the above statements, the breakdown of the SOR in the present study should not be interpreted as the effect of the glassy-stress contribution, but as the true deviation from the linear relationship between structural and rheological responses to strong flow fields. In a sense, we might even consider the deviation of the SOR with increasing shear rate as caused by the increase in a 'glassy-like' contribution coming from an effective 'freezing' behavior of relatively longer relaxation-time modes in response to the applied flow field. A quantitative description of this consideration might be quite informative to this subject. On the other hand, it would be very interesting in a future study to investigate the general trend of the glassy contribution to the birefringence using linear/nonlinear polyethylene melts of various chain lengths (and the side-chain length in the case of nonlinear polymers) over a wide range of temperatures.

Conclusions

In this article, we presented in detail the results of a simulation-based examination of the stress–optical behavior of a linear, short-chain polyethylene melt, $C_{50}H_{102}$, under shear. We have presented a derivation of the generalized Clausius–Mossotti formula for anisotropic media. Four important second-rank tensors, the stress tensor, birefringence tensor, conformation tensor, and orientation tensor, were calculated directly from simulations at various shear rates and compared with each other. We summarize below several main conclusions drawn from the present work.

A linear relationship between the stress and birefringence (SOR) appears to be valid up to a certain shear rate well beyond the incipient point of shear thinning. In the present system, the critical shear stress for shear thinning and the breakdown of the SOR were found to be 3.2 and 5.5 MPa, respectively.

The slopes of the birefringence vs stress curves appeared to decrease with increasing stress for all three quantities (*xx–yy*, *yy–zz*, and *xy*), consistent with many existing experimental results (Matsumoto and Bogue 1977; Janeschitz-Kriegl 1983; Venerus et al. 1999).

The orientation angles obtained from each of the four tensors (σ, n, $\tilde{c}$, and u) were shown to be close to each other at low strain rates but became more and more distinct as shear rate increased. This implies that the principal frame of reference of each tensor does not coincide with that of the other tensors, in general (except for $\tilde{c}$ and u), thus indicating a narrow Gaussian distribution of the chain end-to-end distance.

Rather surprisingly at first, even n and $\tilde{c}$ (also u as well) were shown to be nonlinear at high shear stress values. The critical stress value for the onset of nonlinearity was approximately the same as that at which breakdown of the SOR occurred.

The customary view that the SOR breaks down because of the saturation of chain extension and orientation was demonstrated to be incorrect under shear because the failure of the SOR was observed to occur at a much earlier stage in both chain extension and orientation. Specifically, the chain extension at the point of breakdown of the SOR was about 27% of the full extension (see Fig. 3) and the orientation angle of the birefringence was 23°.

Acknowledgments This research used resources of the Center for Computational Sciences at Oak Ridge National Laboratory, through the University of Tennessee Computational Sciences Initiative. Additional support for CB was provided by the University of Tennessee Computational Sciences Initiative. ORNL is operated for the DOE by UT-Battelle, LLC, under contract number DE-AC0500OR22725.

References

Allen MP, Tildesley DJ (1987) Computer simulation of liquids. Clarendon, Oxford

Baig C, Edwards BJ, Keffer DJ, Cochran HD (2005) Rheological and structural studies of liquid decane, hexadecane, and tetracosane under planar elongational flow using nonequilibrium molecular dynamics simulations. J Chem Phys 122:184906

Baig C, Edwards BJ, Keffer DJ, Cochran HD, Harmandaris VA (2006) Rheological and structural studies of linear polyethylene melts under planar elongational flow using nonequilibrium molecular dynamics simulations. J Chem Phys 124:084902

Beris AN, Edwards BJ (1994) Thermodynamics of flowing systems. Oxford Univ. Press, New York

Bird RB, Armstrong RC, Hassager O (1987) Dynamics of polymeric liquids, vol. 1: fluid mechanics (2nd edn.). Wiley, New York

Bower DI (2002) An introduction to polymer physics. Cambridge Univ. Press, Cambridge

Cormier RJ, Callaghan PT (2002) Molecular weight dependence of segmental alignment in a sheared polymer melt: a deuterium nuclear magnetic resonance investigation. J Chem Phys 116:10020–10029

Cui ST, Cummings PT, Cochran HD (1996a) Multiple time step nonequilibrium molecular dynamics simulation of the rheological properties of liquid n-decane. J Chem Phys 104:255–262

Cui ST, Gupta SA, Cummings PT, Cochran HD (1996b) Molecular dynamics simulations of the rheology of normal decane, hexadecane, and tetracosane. J Chem Phys 105:1214–1220

de Jong S, Groeneweg F, van Voorst Vader F (1991) Calculation of the refractive indices of molecular crystals. J Appl Cryst 24:171–174

Doi M, Edwards SF (1986) The theory of polymer dynamics. Oxford Univ. Press, New York

Evans DJ, Morriss GP (1990) Statistical mechanics of nonequilibrium liquids. Academic, New York

Flory PJ (1969) Statistical mechanics of chain molecules. Wiley, New York

Gao J, Weiner JH (1994) Monomer-level description of stress and birefringence relaxation in polymer melts. Macromolecules 27:1201–1209

Griffiths DJ (1999) Introduction to electrodynamics (3rd edn.). Prentice-Hall, New Jersey
Hoover WG (1985) Canonical dynamics: equilibrium phase–space distributions. Phys Rev A 31:1695–1697
Inoue M, Urano K (1976) Clausius–Mossotti formula for anisotropic dielectrics. J Chem Phys 66:791–794
Inoue T, Okamoto H, Osaki K (1991) Birefringence of amorphous polymers. 1. Dynamic measurement on polystyrene. Macromolecules 24:5670–5675
Inoue T, Mizukami Y, Okamoto H, Matsui H, Watanabe H, Kanaya T, Osaki K (1996) Dynamic birefringence of vinyl polymers. Macromolecules 29:6240–6245
Inoue T, Onogi T, Yao M-L, Osaki K (1999) Viscoelasticity of low molecular weight polystyrene: separation of rubbery and glassy components. J Polym Sci Polym Phys Ed 37:389–397
Inoue T, Onogi T, Osaki K (2000) Dynamic birefringence of oligostyrene: a symptom of "polymeric" mode. J Polym Sci Polym Phys Ed 38:954–964
Janeschitz-Kriegl H (1983) Polymer melt rheology and flow birefringence. Springer, Berlin
Kotaka T, Kojima A, Okamoto M (1997) Elongational flow opto-rheometry for polymer melts. 1. Construction of an elongational flow opto-rheometer and some preliminary results. Rheol Acta 36:646–656
Kröger M, Loose W, Hess S (1993) Rheology and structural changes of polymer melts via nonequilibrium molecular dynamics. J Rheol 37:1057–1079
Kröger M, Luap C, Muller R (1997) Polymer melts under uniaxial elongational flow: stress–optical behavior from experiments and nonequilibrium molecular dynamics computer simulations. Macromolecules 30:526–539
Luap C, Müller C, Schweizer T, Venerus DC (2005) Simultaneous stress and birefringence measurements during uniaxial elongation of polystyrene melts with narrow molecular weight distribution. Rheol Acta 45:83–91
Matsumoto T, Bogue DC (1977) Stress birefringence in amorphous polymers under nonisothermal conditions. J Polym Sci Polym Phys Ed 15:1663–1674
Mavrantzas VG, Theodorou DN (2000a) Atomistic simulation of the birefringence of uniaxially stretched polyethylene melts. Comput Theor Polymer Sci 10:1–13
Mavrantzas VG, Theodorou DN (2000b) Atomistic Monte Carlo simulation of steady-state uniaxial elongational flow of long-chain polyethylene melts: dependence of the melt degree of orientation on stress, molecular length and elongational strain rate. Macromol Theory Simul 9:500–515
Meissner J, Hostettler J (1994) A new elongational rheometer for polymer melts and other highly viscoelastic liquids. Rheol Acta 33:1–21
Moore JD, Cui ST, Cochran HD, Cummings PT (2000) A molecular dynamics study of a short-chain polyethylene melt. I. Steady-state shear. J Non-Newton Fluid Mech 93:83–99
Morrison FA (2001) Understanding rheology. Oxford Univ. Press, New York
Muller R, Froelich D (1985) New extensional rheometer for elongational viscosity and flow birefringence measurements: some results on polystyrene melts. Polymer 26:1477–1482
Muller R, Pesce JJ (1994) Stress–optical behaviour near the T_g and melt flow-induced anisotropy in amorphous polymers. Polymer 35:734–739
Nosé S (1984a) A molecular dynamics method for simulations in the canonical ensemble. Mol Phys 52:255–268
Nosé S (1984b) A unified formulation of the constant temperature molecular dynamics methods. J Chem Phys 81:511–519
Okamoto M, Kojima A, Kotaka T, Münstedt H (1998) Elongational flow birefringence of reactor-made linear low-density polyethylene. Macromolecules 31:5158–5159
Osaki K, Inoue T (1996) Limitation of stress–optical rule for polymeric liquids. Macromolecules 29:7622–7623
Palierne J-F (2004) Rheothermodynamics of the Doi–Edwards reptation model. Phys Rev Lett 93:136001
Siepmann JI, Karaborni S, Smit B (1993) Simulating the critical behavior of complex fluids. Nature 365:330–332
Treloar LRG (1975) The physics of rubber elasticity. Oxford Univ. Press, New York
Tuckerman M, Berne BJ, Martyna GJ (1992) Reversible multiple time scale molecular dynamics. J Chem Phys 97:1990–2001
Urano K, Inoue M (1976) Clausius–Mossotti formula for anisotropic dielectrics. J Chem Phys 66:791–794
van Meerveld J (2004) Validity of the linear stress optical rule in mono-, bi- and polydisperse systems of entangled linear chains. J Non-Newton Fluid Mech 123:259–267
Venerus DC, Zhu S-H, Öttinger HC (1999) Stress and birefringence measurements during the uniaxial elongation of polystyrene melts. J Rheol 43:795–813
Vuks MF (1966) Determination of the optical anisotropy of aromatic molecules from the double refraction of crystals. Opt Spectrosk 20:361–368